Corrected short paper for the *Journal of the Chinese Institute of Engineers*

AUTOMATED TRACKING OF LIQUID VELOCITIES IN A REFRACTIVE INDEX MATCHED POROUS MEDIUM

Michelle Y. F. Huang[1], Alice Y. L. Huang[1], Rong-Her Chen[1], and Hervé Capart[2]

[1] Department of Civil Engineering, National Taiwan University.

[2] Corresponding Author, Dept of Civil Engineering and Hydrotech Res. Institute, National Taiwan University. Tel: 886-2-33664277; Fax: 886-2-23631558; Email: hcapart@yahoo.com.

ABSTRACT

Particle tracking velocimetry is applied to flow inside a porous column at Reynolds number Re = 28. The column is composed of refractive-index-matched solid and liquid materials, allowing seeding particles to be tracked in a laser-illuminated axial slice. To complement earlier results acquired for 7 mm spheres, we conduct new experiments with larger 12 mm spheres. By improving the image acquisition and analysis, we are able to process the new experiments using fully automated algorithms instead of manual tracking. As a result, greater vector yields, more accurate velocity data, and a more complete spatial coverage are achieved.

Key Words: porous media flow; particle tracking velocimetry; refractive index matching.

Subject index: CI6

I. INTRODUCTION

Understanding pore-scale flows in phreatic layers is important to characterize the fate of pollutants, and constitutes a fundamental problem in environmental fluid mechanics. Such flows have been probed in laboratory columns using a variety of optical techniques, including Laser Doppler Anemometry (LDA), Particle Imaging Velocimetry (PIV) and Particle Tracking Velocimetry (PTV). All these techniques require optical access to the interior of the flow cell, achieved by using refractive-index-matched solid and liquid materials (Northrup *et al.*, 1993; Peurrung *et al*., 1995). Recently (Huang *et al.*, 2008), we used laser-illuminated slices through a porous cell to image the full geometry of the pore space in addition to measuring liquid velocities in selected planes. Because of limitations in image quality and processing algorithms, however, particle tracking had to be performed by manual operations.

In the present work, we describe improvements to the method allowing particle tracking to be performed using fully automated algorithms. The improvements include changes to the imaging geometry and sensitivity of the camera, and the adoption of a particle tracking algorithm based on the regularity of particle paths. To complement earlier results obtained for 7 mm spheres, we apply the improved approach to flow through a porous cell packed with 12 mm particles. Compared to previous results, the improved approach yields more numerous velocity measurements of better accuracy and fuller spatial coverage, allowing us to obtain a more reliable estimate of the liquid velocity distribution inside the porous medium.

II. EXPERIMENTAL SETUP

The experiments were conducted using a cylindrical column having a height of 40 cm and a diameter of 5 cm, supplied by a constant head tank. Prior to an experiment, the column was filled with liquid and solid spheres, and bathed in an outer tank filled with liquid to reduce light distortion. The spheres and cylinder are made of polymethyl methacrylate (PMMA), while the liquid selected is called paracymene (Millenium Specialty Chemicals). These solid and liquid materials share the same index of refraction, with the best transparency obtained at temperatures around 15 ºC. The liquid has a density of $\rho = 860$ kg m^{-3}, and viscosity of $\mu = 1.02$ Pa s. Their combination was proposed by Haam *et al.* (2000), and they were earlier used by Hsu and Capart (2007) and Huang *et al.* (2008).

To facilitate comparison with the experiments reported in Huang *et al.* (2008), the flow cell is operated at the same Reynolds number, defined as

$$Re = \frac{\rho D Q}{\mu A \varepsilon} \quad , \tag{1}$$

where D is the diameter of the spheres, A is the cross-section area of the tube, ε is the porosity, and Q is the flow rate. The porosity ε is the ratio of the liquid volume within the flow cell to the total internal volume of the cell. The liquid volume is estimated by subtracting the joint volume of all the solid spheres from the cell internal volume. This yields value $\varepsilon = 0.46$ for the present tests with 12 mm spheres, close to the value $\varepsilon = 0.48$ obtained for our previous

experiments with 7 mm spheres. The flow rate Q, on the other hand, is measured by collecting the liquid outflow at the cell outlet. In the present experiments, we let the flow rate take the value $Q = 2.47$ ml s^{-1}, compared to 4.60 ml s^{-1} for the previous tests. This reduced flow rate is chosen to compensate for the larger size of the spheres (12 mm instead of 7 mm), and maintain the same value of the Reynolds number Re = 28. Steady state was checked by measuring the flow rate again after the experiments.

The measurement configuration is illustrated in Fig. 1. To capture an axial slice through the flow cell, the set-up was illuminated from the side by a laser light sheet, the power of which was increased to 4.5 W for the new experiments (as compared to 0.25 W for the earlier tests). The flow was then imaged through the front using a Charge Coupled Device (CCD) camera (Vision Research Inc.). The highly light-sensitive camera was operated at 50 frames per second (as compared to 10 frames per second for the earlier tests) and a resolution of 800 by 600 pixels, yielding a pixel size of about 0.125 mm for the field of view chosen. In contrast with previous work, the camera is oriented perpendicular to the laser plane (instead of obliquely) to reduce image distortion and keep the whole slice in focus. Prior to velocity measurements, the liquid supply upstream of the cell was seeded with tracer micro-particles (Polyamide Seeding Particles; Dantec Dynamics; diameter 50 μm, density 1.03 g cm^{-3}) imaged as bright speckles on the laser-illuminated frames. Artificial long exposures images of the resulting footage are presented in Fig. 2, which record particle motions as bright pathlines.

Comparison between the previous (Fig. 2(a)) and new experiments (Fig. 2(b)) illustrates the improved image quality. In the next section, we describe the automated methods adopted to track the laser-illuminated micro-particles. A companion paper (Huang *et al.*, 2009) describes measurements of the three-dimensional positions of the packed spheres, obtained to an accuracy of 0.7 mm and 0.3 mm, respectively, for the experiments with 7 mm and 12 mm spheres.

III. IMAGE PROCESSING AND PARTICLE TRACKING

Image sequences acquired in the above configuration were processed as follows. First, the brightness of successive frames was equalized to correct for illumination fluctuations. Images were then analyzed in blocks of 10 successive frames. Before tracking, the stationary background was removed by subtracting an average of the 200 frames preceding the image block of interest. After convolution with a Laplacian-of-Gaussian (LoG) filter, the moving tracer particles were identified as brightness maxima on the convoluted images. After identifying such maxima, their positions were refined to sub-pixel accuracy using local quadratic fits (see Capart *et al.*, 2002).

To obtain well-resolved velocities, we chose high seeding concentrations (hence tracer particles close to each other) which made nearest neighbor tracking unreliable. Due to high flow deformations, and because particles come in an out of view as they enter and leave the

laser-illuminated plane (see Fig. 2), patterns of neighboring particles were also insufficiently stable to apply pattern-based tracking methods. Robust tracking could be performed, however, on the basis of the path regularity indicator proposed in Capart *et al.* (2002). Two particles of indices i and j and positions $\boldsymbol{r}_i^{(k)}$ and $\boldsymbol{r}_j^{(k+1)}$ on two successive frames k and k+1 were judged to constitute good matches if their path distance d_{ij} was small, where the path distance is the indicator of path regularity defined by

$$d_{ij} = \max(d_{ij}^{(-)}, d_{ij}^{(+)}) . \tag{2}$$

In this expression, $d_{ij}^{(-)}$ and $d_{ij}^{(+)}$ denote distances between extrapolated particle positions and their nearest neighbors on frames $k-1$ and $k+2$ of the sequence, *i.e.*

$$d_{ij}^{(-)} = \min_m \left\| \boldsymbol{r}_{ij}^{(-)} - \boldsymbol{r}_m^{(k-1)} \right\|, \qquad d_{ij}^{(+)} = \min_n \left\| \boldsymbol{r}_{ij}^{(+)} - \boldsymbol{r}_n^{(k+2)} \right\|, \tag{3}$$

where $\boldsymbol{r}_{ij}^{(-)}$ and $\boldsymbol{r}_{ij}^{(+)}$ are the backward and forward extrapolations

$$\boldsymbol{r}_{ij}^{(-)} = \boldsymbol{r}_i^{(k)} - (\boldsymbol{r}_j^{(k+1)} - \boldsymbol{r}_i^{(k)}) , \qquad \boldsymbol{r}_{ij}^{(+)} = \boldsymbol{r}_i^{(k)} + 2(\boldsymbol{r}_j^{(k+1)} - \boldsymbol{r}_i^{(k)}) . \tag{4}$$

To accelerate the repeated identification of nearest neighbors, an efficient Delaunay search algorithm was used (Preparata and Shamos, 1985). Particles on two successive frames k and $k+1$ are characterized by a short path distance if both their forward and backward extrapolated displacements fall close to particles identified on frames $k-1$ and $k+2$. Using the optimization procedure described in Capart *et al.* (2002), path distances d_{ij} were used to choose the most likely matches, and to screen out candidate matches with path distances that exceeded a certain threshold $d_{\max}$. The standard Euclidean distance $\left\| \boldsymbol{r}_j^{(k+1)} - \boldsymbol{r}_i^{(k)} \right\|$ was also

used to screen out pairs of candidates which were too far from each other. Although this principle allows mostly correct tracks to be assembled over successive image frames, a few outliers remain. We eliminate them by requiring that particle tracks satisfy the path regularity criterion $d_{ij} < d_{\max}$ over at least five successive frames.

The velocity vectors derived from these particle tracks must be converted from pixel coordinates to physical coordinates. This is done by projecting particle positions from the image plane back onto the laser-illuminated plane. The method adopted follows Douxchamps *et al.* (2005), and involves the computation of ray-plane intersections based on a calibrated camera viewpoint. Once converted back to physical coordinates, the vectors can also be plotted jointly with solid sphere outlines derived from the geometry measurements described in the companion paper (Huang *et al.*, 2009). To evaluate flow statistics, the velocity vectors can finally be binned into the square cells of a mesh grid, with no value assigned to empty cells.

IV. PARTICLE TRACKING RESULTS

Particle tracking results obtained using the previous manual approach (Huang *et al.*, 2008), and the present automated algorithms are compared in Fig. 3. Both sets of flow vectors agree qualitatively with the corresponding long exposure images (Fig. 2). The new results (Fig. 3(b)), however, feature various important improvements compared to the previous

measurements (Fig.3(a)). First, the use of automated techniques permits increased vector yields (9823 vectors obtained automatically instead of 3757 vectors obtained by painstaking manual analysis for the previous experiments). Secondly, the spatial coverage of the measurements is much improved for the new results. Whereas the previous data (Fig. 3(a)) feature numerous gaps (zones where no velocity vectors were identified), the new results provide a nearly complete coverage of the liquid domain, including low velocity zones of the flow field.

To perform a more rigorous comparison, we applied both the manual and automated techniques to the experiment with 12 mm spheres. For this purpose, we selected a square sub-window of the flow field, corresponding to x and z coordinates in the ranges $-2.5 < x < 0$ and $-2.5 < z < 0$ (dimension in cm). Using the manual techniques described in Huang *et al.* (2008), 736 velocity vectors were harvested from this sub-window. For comparison, we also extracted 736 velocity vectors from the automatically acquired flow field of Fig. 3(b). The resulting vectors are plotted in Fig. 4(a) and 4(b). Although both techniques were applied to the same video footage, the results again underline the higher quality and more uniform coverage that can be attained using the automated methods.

In Fig. 4(c) and 4(d), we compare the binned velocity components obtained using the two techniques. The results from the two different methods fall near the line of perfect agreement for the u and w components, indicating that both methods yield consistent results.

The manually acquired vectors, however, exhibit two artifacts. First, their components *u* and *v* cluster around quantized displacements associated with integer pixel displacements. Secondly, manual vectors appear to be slightly biased towards smaller velocity values. This suggests that particles moving more slowly, easier to recognize, are chosen preferentially by the human operator. The automated techniques avoid the first artifact by capturing positions to sub-pixel accuracy. Because the automated algorithms are based on path regularity instead of particle displacements, they should also be immune to the second artifact of velocity bias.

To evaluate the methods in a more quantitative way, we can estimate the magnitude of measurement errors by examining differences between measured velocities and their binned averages (Huang *et al.*, 2008). The resulting errors ε_u and ε_w for velocity components *u* and *w* are listed in Table 1 for the different flow fields discussed above. For the whole-field measurements presented in Fig. 3, automated techniques applied to the experiment with 12 mm spheres yield a more than twofold reduction in error compared to the manual techniques applied to the experiment with 7 mm spheres. For the sub-window shown in Fig. 4, a similar reduction in error is recorded when applying automated instead of manual techniques to the same experiment, in this case conducted with 12 mm spheres.

Because they achieve better coverage and higher accuracy, and also because the liquid flow in the pore network can be better resolved in assemblies of larger spheres, the new measurements allow us to estimate more reliably the velocity distribution inside the porous

medium. Results for the probability density distributions of lateral and vertical velocities are presented in Fig. 5. To compare results from experiments with 7 mm and 12 mm spheres, the velocity data are normalized by the absolute value of the mean downwards velocity $\overline{w}$ = 0.26 cm s^{-1} (the mean lateral velocity, close to zero, cannot be used for this purpose). Data from the previous experiments (7 mm spheres, manual tracking) are plotted using hollow symbols, while the new data (12 mm spheres, automated tracking) are plotted using black dots. The differences observed may be partly due to the change in aspect ratio between the two experiments (different ratios of cylinder diameter to sphere diameter), influencing the corresponding flow fields. Previous experiments and computations (Cenedese and Viotti, 1996; Magnico, 2003), however, indicate that normalized velocity distributions should be in close agreement for flows through porous cells of different aspect ratios, provided that the Reynolds number is the same. The rather large differences observed in Fig. 5, therefore, are likely to be mostly due to changes in the accuracy and spatial coverage of the measurements. The flatter, more diffuse distribution characterizing our earlier measurements with 7 mm spheres is consistent with contamination by random noise associated with greater velocity measurement errors. Likewise, the under-representation of low velocities in that case is likely due to the under-sampling of low velocity regions near the solid spheres and in certain regions of the pore space.

V. CONCLUSION

In the present work, we have presented improved particle tracking velocimetry measurements for liquid flow inside a porous assembly of spheres. By applying automated techniques to footage of higher quality, we found that considerable gains in coverage and accuracy could be achieved. The automated algorithms are able to position particles more accurately, and to track them more reliably using a criterion based on path regularity. Moreover, they are able to better resolve zones of low velocity in certain regions of the pore space, which appear to be under-sampled by manual methods. This results in a more reliable estimate of the distribution of velocities inside the porous medium.

REFERENCES

Capart, H., Young D. L., and Zech, Y., 2002, "Voronoï Imaging Methods for the Measurement of Granular Flows," *Experiments in Fluids*, Vol. 32, pp. 121-135.

Cenedese, A., and Viotti, P., 1996, "Lagrangian Analysis of Nonreactive Pollutant Dispersion in Porous Media by Means of the Particle Image Velocimetry Technique," *Water Resources Research*, Vol. 32, No. 8, pp. 2329-2343.

Douxchamps, D., Devriendt, D., Capart, H., Craeye, C., Macq, B., and Zech, Y., 2005, "Stereoscopic and Velocimetric Reconstructions of the Free Surface Topography of Antidune Flows," *Experiments in Fluids*, Vol. 39, No. 3, pp. 533-551.

Haam, S. J., Brodkey, R. S., Fort, I., Klaboch, L., Placnik, M., and Vanecek, V., 2000, "Laser Doppler Anemometry Measurements in an Index of Refraction Matched Column in the Presence of Dispersed Beads – Part I," *International Journal of Multiphase Flow*, Vol. 26, pp. 1401-1418.

Hsu, H. C., and Capart, H., 2007, "Enhanced Upswing in Immersed Collisions of Tethered Spheres," *Physics of Fluids*, Vol. 19, No. 10, Art. No. 101701.

Huang, A. Y. L., Huang, M. Y. F., Capart, H., and Chen, R. H., 2008, "Optical Measurements of Pore Geometry and Fluid Velocity in a Bed of Irregularly Packed Spheres," *Experiments in Fluids*, Vol. 45, No. 2, pp. 309-321.

Huang, A. Y. L., Huang, M. Y. F., Chen, R. H., and Capart, H., 2009, "Influence of Aspect

Ratio on the Distribution of Porosity and Velocity in Columns of Spheres," *Journal of the Chinese Institute of Engineers*, Vol. 32, No. 3, pp. xx-xx.

Magnico, P., 2003, "Hydrodynamic and Transport Properties of Packed Beds in Small Tube-to-Sphere Diameter Ratio: Pore Scale Simulation Using an Eulerian and a Lagrangian Approach," *Chemical Engineering Science*, Vol. 58, pp. 5005-5024.

Northrup, M. A., Kulp, T. J., Angel, S. M., and Pinder, G. F., 1993, "Direct Measurement of Interstitial Velocity Field Variations in a Porous Medium Using Fluorescent-Particle Image Velocimetry," *Chemical Engineering Science*, Vol. 48, No. 1, pp. 13-21.

Peurrung, L. M., Rashidi, M., and Kulp, T. J., 1995, "Measurement of Porous Medium Velocity Fields and Their Volumetric Averaging Characteristics Using Particle Tracking Velocimetry," *Chemical Engineering Science*, Vol. 50, No. 14, pp. 2243-2253.

Preparata, F. P., and Shamos, M. I., 1985, *Computational Geometry – An Introduction*. Springer-Verlag, Berlin, Germany.

TABLES

Table 1 Estimated errors ε_u and ε_w on velocity components in the *x* and *z* directions, for the manual and automated tracking methods

Coverage	Spheres diameter [mm]	Tracking method	Number of vectors	ε_u [mm/s]	ε_w [mm/s]
Whole field	7	manual	3757	0.58	1.01
	12	automated	9823	0.14	0.41
Sub-window	12	manual	736	0.23	0.53
	12	automated	736	0.12	0.23

FIGURES

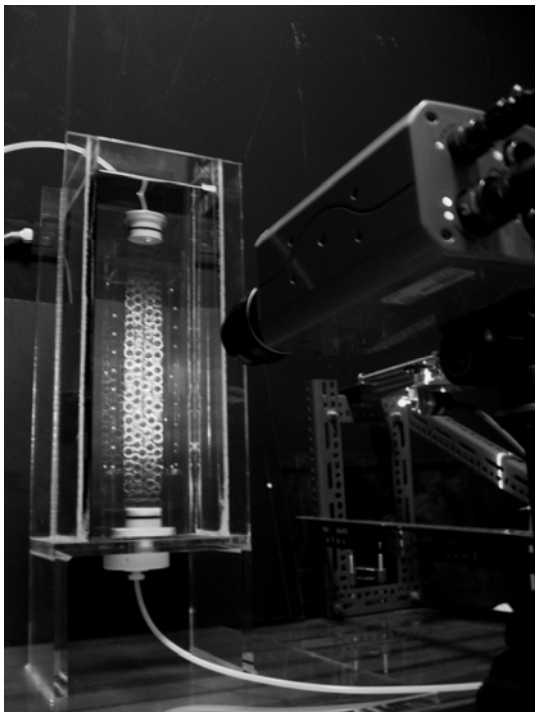

Fig. 1 Experimental setup: a slice through the refractive-index-matched column is illuminated from the side and imaged by a CCD camera

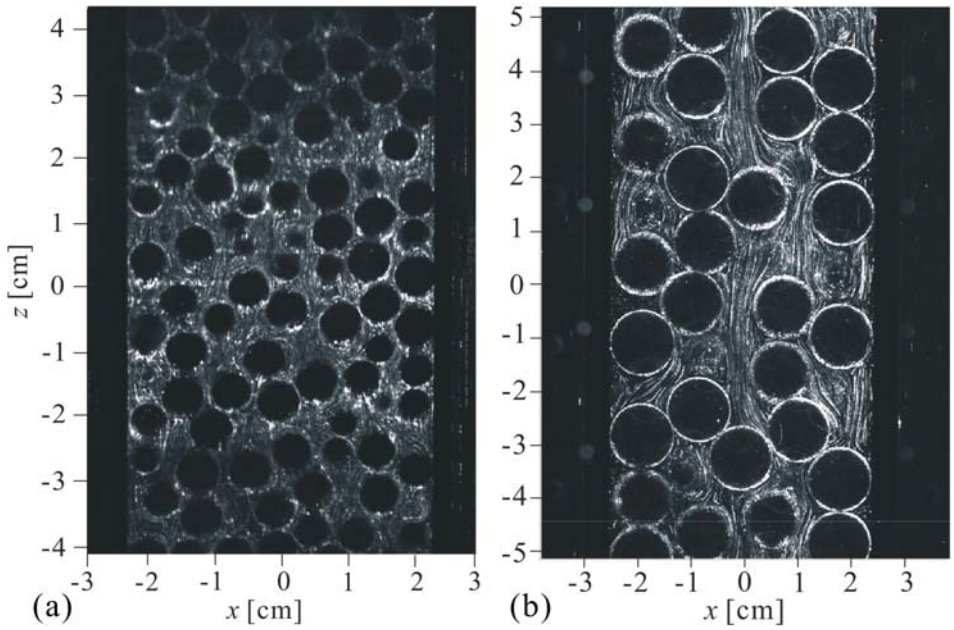

Fig. 2 Long exposure images of the velocimetric plane resampled in spatial coordinates: (a) column packed with 7 mm spheres (Huang *et al*., 2008); (b) column packed with 12 mm spheres (new experiments)

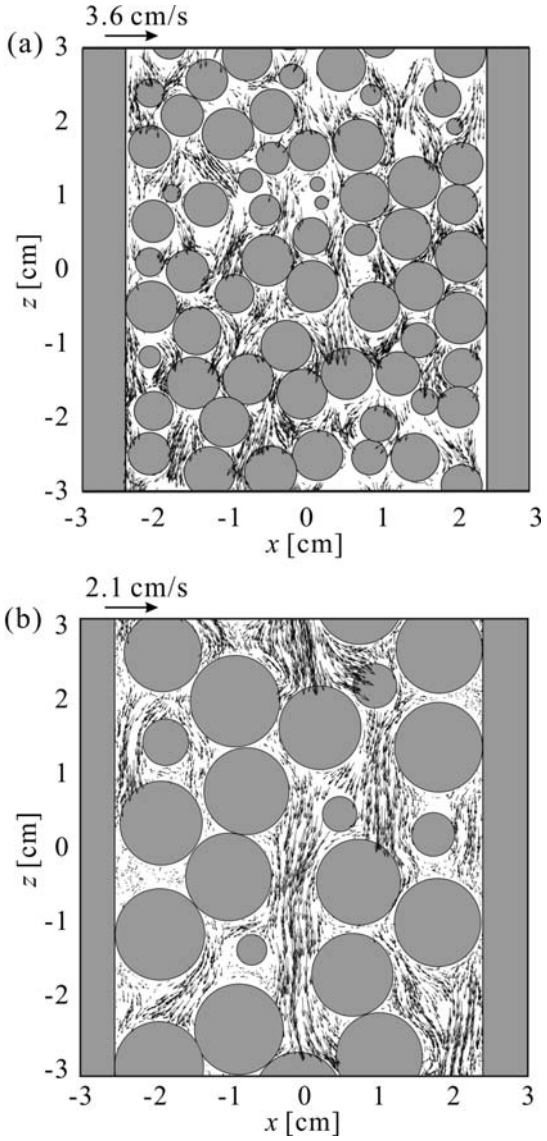

Fig. 3 Measured velocity fields in axial slices through porous assemblies of spheres: (a) 7 mm spheres, manual tracking (Huang *et al.*, 2008); (b) 12 mm spheres, fully automated algorithms (new experiments)

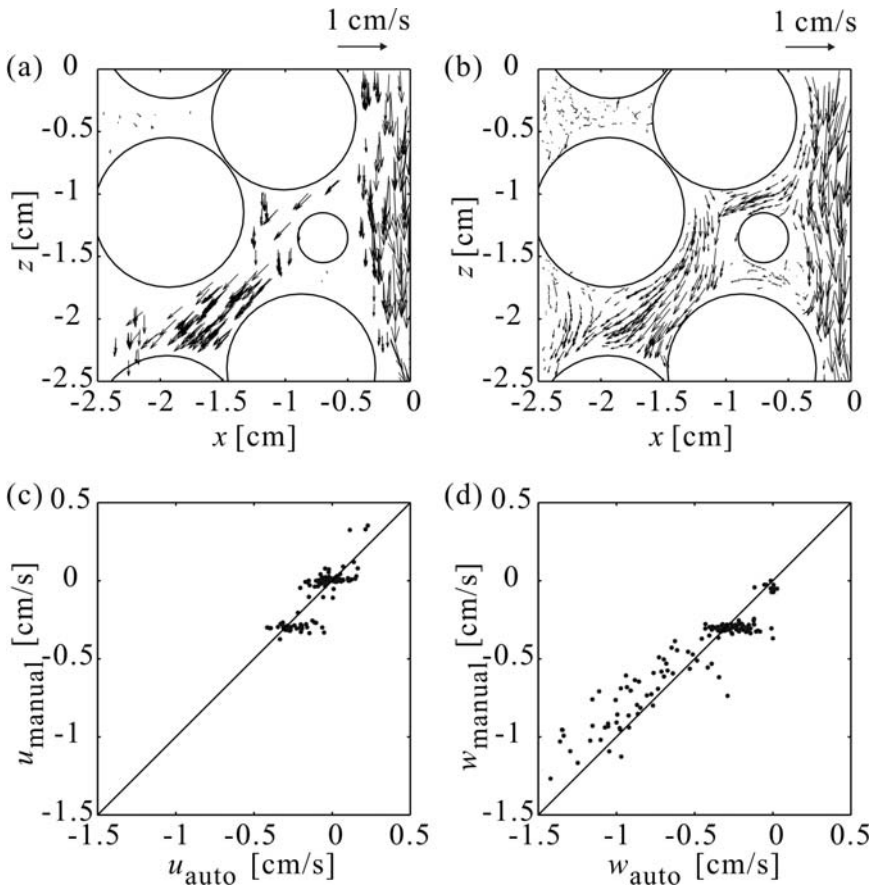

Fig. 4 Manual and automated velocity measurements for a flow sub-window in the centre plane of a column packed with 12 mm spheres (new experiments): (a) velocity vectors captured by manual technique; (b) velocity vectors captured by automated technique; (c) comparison of manual and automated measurements for velocity component *u* (spatial bin averages); (c) comparison of manual and automated measurements for velocity component *w* (spatial bin averages). For clarity, only subsets of the acquired vectors are plotted in panels (a) and (b).

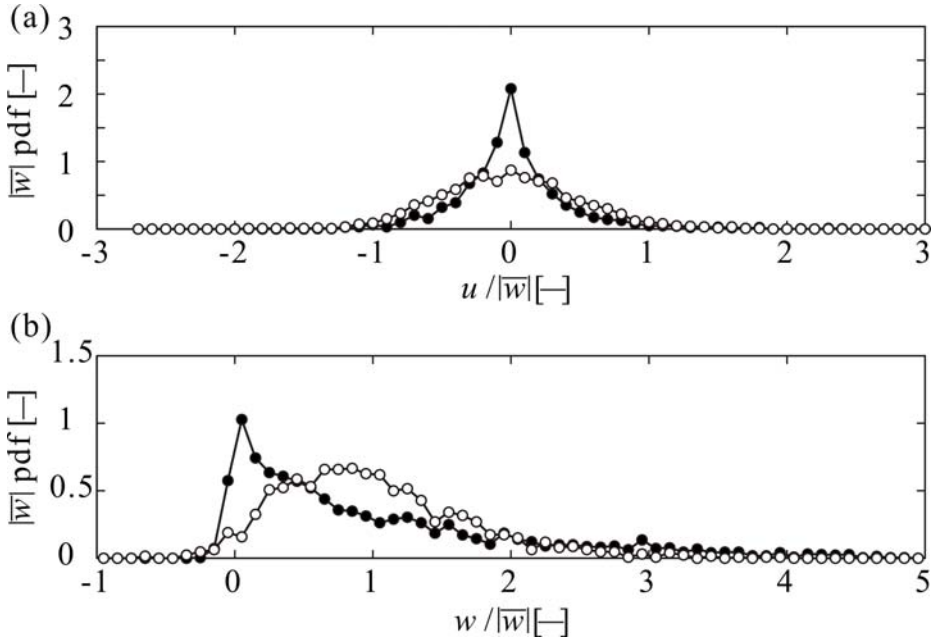

Fig. 5 Probability density distributions of liquid velocities in columns packed with 7 mm (hollow symbols) and 12 mm spheres (black dots): (a) lateral velocity distribution; (b) vertical velocity distribution, both normalized with respect to the absolute value of the mean downwards velocity $\overline{w}$